Experimental and numerical modeling of thermally-induced ratcheting displacement of geomembranes on slopes

Article *in* Geosynthetics International · December 2014

DOI: 10.1680/gein.14.00021

CITATIONS
2

READS
159

2 authors:

Cesar Pasten
University of Chile
33 PUBLICATIONS **152** CITATIONS
SEE PROFILE

J. Carlos Santamarina
King Abdullah University of Science and Tech…
272 PUBLICATIONS **5,674** CITATIONS
SEE PROFILE

Experimental and numerical modeling of thermally-induced ratcheting displacement of geomembranes on slopes

C. Pasten[1] and J. C. Santamarina[2]

[1]*Assistant Professor, Department of Civil Engineering, University of Chile, Av. Blanco Encalada 2002, Santiago 8370449, Chile, Telephone: +56 2 2978 4643; Telefax: +56 2 2671 8788; E-mail: cpasten@ing.uchile.cl*
[2]*Professor, School of Civil and Environmental Engineering, Georgia Institute of Technology, 790 Atlantic Drive NW, Atlanta, Georgia, 30332-0355, USA, Telephone: +1 404 894 7605; Telefax: +1 404 894 2281; E-mail: jcs@gatech.edu*

Received 20 May 2014, revised 25 August 2014, accepted 28 August 2014

ABSTRACT: Exposed geomembranes are subjected to thermal cycles of relatively high amplitude. In the present study, the behavior of exposed geomembranes on inclined planes subjected to thermal cycles was investigated using experimental and numerical methods. Experimental results corroborated the emergence of thermally-driven displacement accumulation, or ratcheting, which was inversely proportional to the static factor of safety. The complementary numerical study considered the thermo-elastic membrane properties, constant temperature change amplitude, and an elastic-perfectly plastic constitutive model with a critical elastic threshold displacement for the membrane–soil interface. Results show that thermally-induced ratcheting displacements increased as the static factor of safety decreased, in agreement with experimental observations, and as the ratio between the unconstrained thermal elongation of the geomembrane and the critical elastic interface displacement increased.

KEYWORDS: Geosynthetics, Exposed geomembranes, Ratcheting, Thermal cycles

REFERENCE: Pasten, C. & Santamarina, J. C. (2014). Experimental and numerical modeling of thermally-induced ratcheting displacement of geomembranes on slopes. *Geosynthetics International*, **12**, No. 6, 334–341. [http://dx.doi.org/10.1680/gein.14.00021]

1. INTRODUCTION

Geomembranes are semi-impermeable, polymeric sheets that can remain exposed either during construction or as part of a permanent geomembrane cover system (Richardson 2000; Rowe 2005). Laboratory studies of small sample area and small- to medium-scale field studies have shown that an exposed geomembrane heated by direct sun radiation can undergo temperature changes as high as 50°C depending on its color and the season (Pelte *et al.* 1994; Rowe 2005; Rowe *et al.* 2012a; Take *et al.* 2012). The thermal expansion is constrained by friction against the underlying soil. Low flexural stiffness, high thermal expansion, and frictional restraint lead to the formation of wrinkles, especially at imperfections such as creases, seams, and overlaps (Giroud and Morel 1992; Take *et al.* 2007; Rowe 2011), and may induce gradual slippage when geomembranes are placed on slopes.

In order to investigate the behavior of exposed geomembranes subjected to temperature cycles, a physical model that consisted of an unrestrained smooth geomembrane resting on an inclined plane, housed in a temperature-controlled container was fabricated. First, experimental evidence of thermally-induced ratcheting displacement is presented and then governing equations are identified to formulate a numerical algorithm that solves the coupled thermo-mechanical problem.

2. EXPERIMENTAL EVIDENCE OF GEOMEMBRANE RATCHETING DISPLACEMENT

The experimental setup consisted of a transparent low-density polyethylene (LDPE) membrane resting on an inclined aluminum base. Values of the geomembranes's unit weight, Young's modulus, and thermal expansion coefficient were adopted from the membrane manufacturer (parameters are summarized in Table 1). The slope-membrane system was housed within a thermally insulated

Table 1. Experimental geomembrane parameters

Parameter	Symbol	Units	Value[a]
Length	L	m	0.16
Width	B	m	0.08
Thickness	t_h	mm	0.5
Young's modulus[b]	E	GPa	0.3
Unit weight[b]	γ_m	kN/m^3	9.5
Thermal expansion coefficient[b]	α	10^{-5}/°C	18

Note: [a] Values are also used in the numerical verification. [b] Values adopted from the geomembrane manufacturer.

box with controlled air temperature. The air temperature was recorded every 5 s using two thermocouples mounted near the membrane's longitudinal edges and a data logger system. Metal shields prevented direct source radiation to the membrane and sensors, and a fan ensured air circulation and thermal homogenization (Figure 1). Membrane displacements were monitored every 5 min with a digital camera mounted parallel to the inclined base outside the insulating box (pixel size = 0.03 mm). The membrane displacement was determined by image-processing techniques using marks painted on the membrane.

2.1. Experimental results

A typical test comprised three stages: (i) stabilization (2 h), (ii) thermal cycles (~10 h), and (iii) cooling (~6 h). Thermal cycles imposed by a thermostat inside the insulating box resulted in a temperature amplitude $\Delta T = 8$°C near the lower and upper edges of the membrane and a constant period $P = 34$ min. The maximum temperature during the tests was set to 50°C to prevent damage in the polyethylene junctions of the insulated box, thermocouple cables, and supporting structures. On the other hand, the minimum temperature, 32°C, was controlled by a light bulb that remained on to provide illumination during photo shootings inside the insulated container. Air temperature and the displacement of points near the lower and upper edges of the membrane are shown in Figure 2 for base inclinations $\eta = 20°$, 24°, and 29°.

The initial temperature increase ($\Delta T \sim 15$°C above room temperature) expands the membrane. The measured elongation $\Delta L = 0.36$ mm (Figure 2) is comparable with the computed free thermal elongation $\Delta L = \alpha \cdot \Delta T \cdot L$

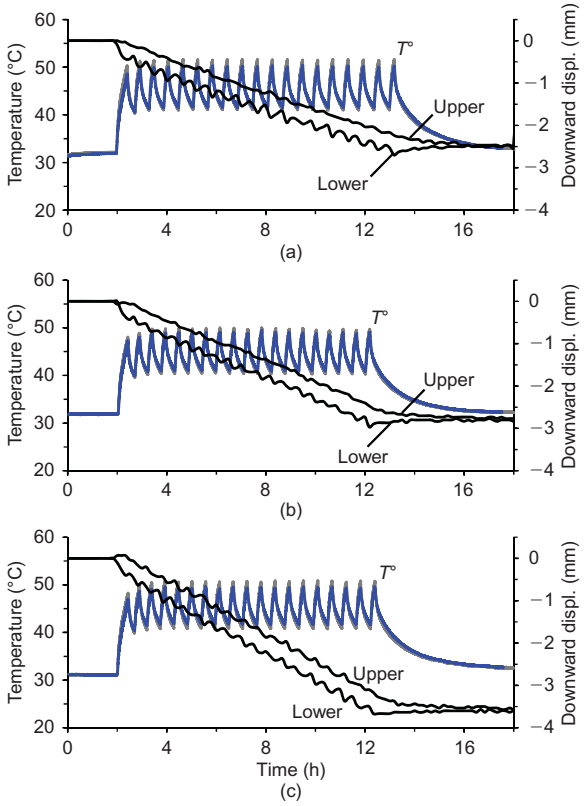

Figure 2. Thermally-induced geomembrane ratcheting displacement for various base inclination angles η: (a) $\eta = 20°$; (b) $\eta = 24°$; (c) $\eta = 29°$. Air temperature $T°$ is measured by two thermocouples (refer to Figure 1). Displacements at points near the lower and upper edges of the membrane are determined by image processing. Displacement precision is 0.03 mm

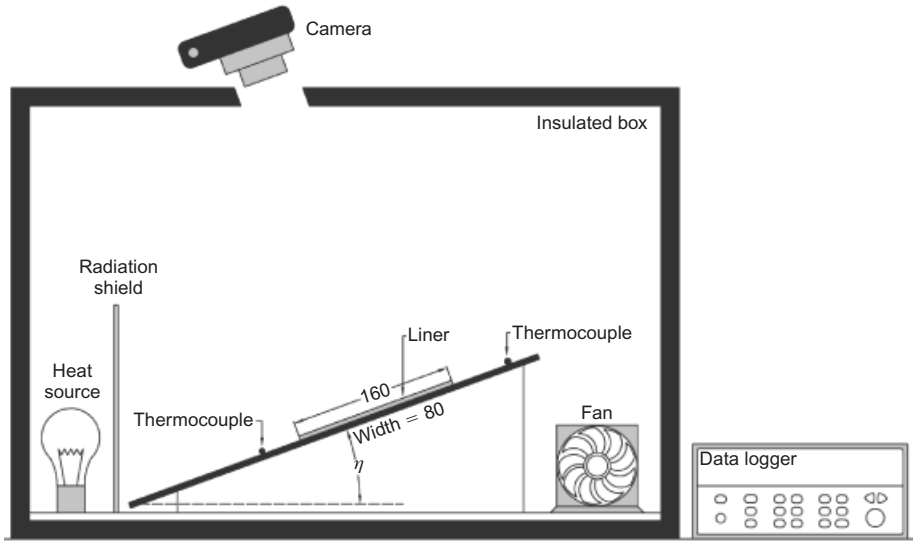

Figure 1. Thermally-induced geomembrane ratcheting displacement: experimental setup. Dimensions are in millimeters

(for $\alpha = 1.8 \cdot 10^{-4}°C^{-1}$). Additional temperature changes cause expansions and contractions that correlate with the heating and the cooling phases, resulting in membrane ratcheting displacement. The rate of accumulated displacement increases with the base inclination η and is linearly related to the number of thermal cycles (Figure 2).

3. NUMERICAL ALGORITHM FOR CYCLIC THERMAL LOADING

The next step is to analyze the thermally-induced ratcheting displacement of the membrane to identify the governing equations.

3.1. Global static equilibrium

Consider a geomembrane with longitudinal length L (m), width B (m), thickness t_h (m), and unit weight γ_m (N/m^3) resting on a plane inclined at an angle η (°). Equilibrium requires that the shear stress τ (Pa) induced by the geomembrane weight along the inclined plane is less than or equal to the shear strength τ_{max} (Pa) of the geomembrane–base interface. The component of the weight parallel to the plane causes a mean shear stress τ (Pa)

$$\tau = \gamma_m \cdot t_h \cdot \sin\eta \leqslant \tau_{max} = \mu \cdot \gamma_w \cdot t_h \cdot \cos\eta \quad (1)$$

where μ (–) is the interface friction coefficient. Then, the static global factor of safety is

$$FS = \frac{\tau_{max}}{\tau} = \frac{\mu}{\tan\eta} \quad (2)$$

3.2. Element-level equilibrium and compatibility

Repeated heating and cooling cycles alter the geomembrane static equilibrium. The geomembrane is discretized into N elements of length $L_0 = L/N$ (m). The ith-element experiences a downslope relative displacement δ_i (m) at its higher edge and δ_{i+1} (m) at its lower edge (Figure 3a).

Force equilibrium requires the longitudinal force on the ith-element upper edge Q_i (N) plus the weight component parallel to the plane $W_i \cdot \sin\eta = (\gamma_m \cdot t_h \cdot L_0 \cdot B \cdot \sin\eta)$ equals the sum of the longitudinal force on its lower edge Q_{i+1} (N) and the shear force at the base interface S_i (N) (Figure 3a)

$$Q_i = Q_{i+1} + S_i - W_i \cdot \sin\eta \quad (3)$$

The shear force S_i is the shear stress on the ith-element τ_i (Pa) times the element basal area $A_c = B \cdot L_0$ (m^2)

$$S_i = \tau_i \cdot B \cdot L_0 \quad (4)$$

The shear stress τ_i (Pa) is assumed to have a linear elastic-perfectly plastic displacement response

$$\tau_i = \tau_i(\delta_i, \delta_{i+1}) = \begin{cases} -\tau_{max} & \text{if} \quad \delta_i < -\delta^* \\ k \cdot \left(\dfrac{\delta_i + \delta_{i+1}}{2}\right) & \text{if} \quad -\delta^* < \delta_i < \delta^* \\ \tau_{max} & \text{if} \quad \delta_i > \delta^* \end{cases} \quad (5)$$

where the critical elastic interface displacement δ^* (m) (i.e. the displacement required to mobilize the maximum interface shear strength) defines the interface shear stiffness k_j (Pa/m) as

$$k = \frac{\tau_{max}}{\delta^*} \quad (6)$$

Consider a uniform temperature increase throughout the membrane. Thermal expansion of the ith-element is constrained by the longitudinal forces acting on the element. Displacement compatibility requires that the change in

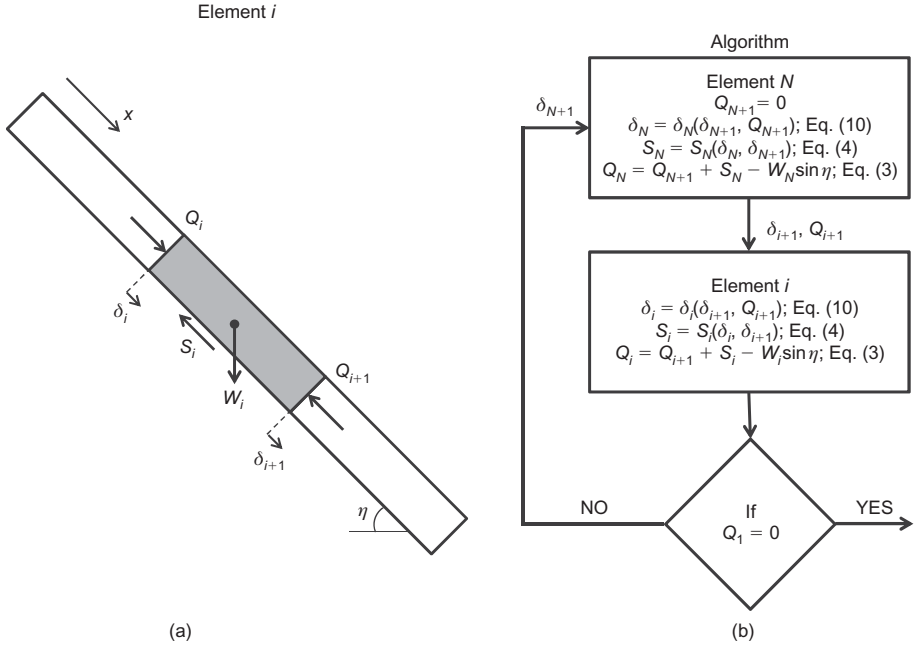

Figure 3. Numerical algorithm for a geomembrane subjected to temperature cycles. (a) Longitudinal forces Q, shear force at the interface S, and relative displacements δ at the top and bottom of the ith element. (b) Solution algorithm. The element weight is $W_i = \gamma_m \cdot t_h \cdot L_0 \cdot B$ (note: parameters are found in Table 1)

element length $\Delta_i = \delta_{i+1} - \delta_i$ (m) equals the free thermal elongation Δ_i^T (m) minus the elastic contraction Δ_i^σ (m)

$$\Delta_i = \delta_{i+1} - \delta_i = \Delta_i^T - \Delta_i^\sigma \tag{7}$$

The free thermal elongation Δ_i^T (m) is a function of the thermal expansion coefficient α (°C^{-1}) and the temperature change ΔT (°C)

$$\Delta_i^T = \alpha \cdot \Delta T \cdot L_0 \tag{8}$$

whereas the elastic contraction of the element Δ_i^σ (m) is inversely proportional to the geomembrane Young's modulus E (Pa)

$$\Delta_i^\sigma = \frac{Q_i + Q_{i+1}}{2} \frac{L_0}{B \cdot t_h \cdot E} \tag{9}$$

Combining equilibrium and compatibility conditions (Equations 3 and 7), the displacement of the ith-element upper edge δ_i can be solved as a function of the ith-element lower edge displacement δ_{i+1} and axial force Q_{i+1}

$$\delta_i(\delta_{i+1}, Q_{i+1}) = \begin{cases} \delta_{i+1} + \dfrac{L_0}{2Bt_hE}(2Q_{i+1} - \tau_{max}BL_0 - W_i \sin\eta) - \Delta_i^T & \text{if } \left(\dfrac{\delta_i + \delta_{i+1}}{2}\right) \leqslant -\delta^* \\ \dfrac{\delta_{i+1}\left(1 + \dfrac{L_0^2 k_i}{4t_hE}\right) + \dfrac{L_0}{Bt_hE}Q_{i+1} - \dfrac{L_0 W_i \sin\eta}{2Bt_hE} - \Delta_i^T}{1 - \dfrac{L_0^2 k_i}{4t_hE}} & \text{if } -\delta^* < \left(\dfrac{\delta_i + \delta_{i+1}}{2}\right) < \delta^* \\ \delta_{i+1} + \dfrac{L_0}{2Bt_hE}(2Q_{i+1} + \tau_{max}BL_0 - W_i \sin\eta) - \Delta_i^T & \text{if } \left(\dfrac{\delta_i + \delta_{i+1}}{2}\right) \geqslant \delta^* \end{cases} \tag{10}$$

3.3. Numerical algorithm

Equations 3 to 10 allow the evolution of geomembrane stresses and displacements during thermal cycles to be computed. The new equilibrium condition for the geomembrane subjected to a constant temperature change ΔT is calculated from the lowest element edge $i = (N + 1)$ to the first edge $i = 1$ at the top of the membrane. The iterative algorithm follows (Figure 3b).

1. Impose a relative displacement at the Nth-element lower edge δ_{N+1} and compute the relative displacement at the Nth-element upper edge δ_N where $Q_{N+1} = 0$ for the free end (Equation 10).
2. Calculate the Nth-element shear force S_N (Equations 4 and 5) and axial force acting at its upper edge Q_N (Equation 3).
3. Use the relative displacement δ_N and the axial force Q_N to equilibrate the element $i = (N - 1)$. Then, continue element-by-element to reach the first element $i = 1$.
4. Verify the updated longitudinal force on the first element upper edge Q_1. If $|Q_1| > \varepsilon$, where ε (N) is a preselected tolerance value, repeat the iterative procedure for a different relative displacement value δ_{N+1} in step 1. If $|Q_1| \leqslant \varepsilon$, the solution has converged.

The initial static condition is obtained using $\Delta_i^T = 0$ in Equation 7, and it results in zero longitudinal force in the membrane and homogeneous shear stress and relative displacement along the membrane-soil interface (Equation 1).

3.4. Numerical results

This numerical algorithm was used to study the behavior of geomembranes subjected to cyclic temperature changes. Thermal effects can be categorized according to the static factor of safety $FS = \mu/\tan\eta$ and the normalized free thermal elongation Δ^T/δ^*, which is the ratio between the unconstrained thermal elongation of the geomembrane $\Delta^T = \alpha \cdot \Delta T \cdot L$ and the critical elastic interface displacement δ^*. The model parameters adopted in this study are shown in Tables 1 and 2. In the absence of experimental interface-specific data, a critical elastic interface displacement $\delta^* = 0.01$ mm was adopted.

3.4.1. *Ratcheting displacement and number of cycles*

Figure 4 shows the membrane upper edge displacement δ_1 as a function of the number of thermal cycles for various factors of safety FS and thermal amplitudes ΔT. The ratcheting displacement (i) evolved linearly with the number of thermal cycles, (ii) increased as the factor of safety decreased, and (iii) increased with the amplitude of thermal cycles. The symbols in Figure 4 correspond to average displacement of the membrane shown in Figure 2.

Table 2. Parameters used in numerical simulation

Parameter	Symbol	Units	Value
Temperature change	ΔT	°C	0 to 40
Base inclination	η	°	0 to 30
Critical elastic interface displacement	δ^*	mm	0.01
Interface friction coefficient[a]	μ	–	0.6

Note: [a] Interface friction angle: $\varphi = \tan^{-1}(0.6) = 31°$ measured as the critical sliding angle on the inclined plane.

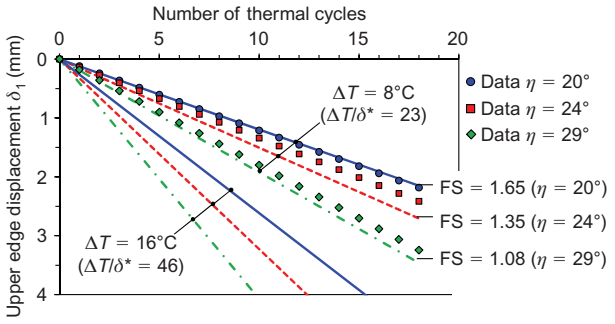

Figure 4. Evolution of membrane upper edge displacement δ_1 with the number of thermal cycles for various factors of safety $FS = \mu/\tan\eta$ and temperature change amplitudes ΔT. Symbols represent the average displacement of the membranes shown in Figure 2. Note: geomembrane and model parameters are found in Tables 1 and 2

The numerical results compare well with the measured displacement rates.

3.4.2. *Load-transfer curves*

Load-transfer curves for a factor of safety $FS = 1.65$ and various normalized free thermal elongations Δ^T/δ^* are shown in Figure 5. The low thermal elongation $\Delta^T/\delta^* = 0.5$ does not cause plastic displacement accumulation because the critical elastic interface displacement is not exceeded anywhere along the geomembrane interface. The intermediate thermal elongation $\Delta^T/\delta^* = 2.0$ accumulates plastic displacement at a limited rate since the critical interface displacement is overcome in less than half of the membrane length. Finally, the large thermal elongation $\Delta^T/\delta^* = 15$ results in accelerated downward membrane ratcheting displacement because the critical interface displacement is exceeded in more than half of the membrane length in both heating and cooling phases. Membrane thermal expansion and contraction cause both a reversal of relative displacements with respect to the 'neutral point' and a linear accumulation of displacements with the number of thermal cycles. In the three cases, the longitudinal normal stress within the membrane $\sigma = Q/(t_h \cdot B)$ and shear stress at the interface τ reverse during a heating–cooling cycle and remain unchanged with subsequent cycles.

3.4.3. *Critical thermal elongation*

Figure 6 summarizes normalized displacements of the membrane upper edge δ_1/L after the first thermal cycle as a function of the normalized free thermal elongation Δ^T/δ^*. Critical thermal elongations that define small, intermediate, and large thermal displacement behaviors are $\Delta^T/\delta^* = 0.9$ and $\Delta^T/\delta^* = 3.2$ for a static factor of safety $FS = 1.65$. Displacement accumulation exacerbates at large thermal displacements with the number of cycles. Critical values decrease as the factor of safety decreases. In other words, membranes with smoother membrane–soil interfaces and steeper base inclinations require lower thermal amplitudes to experience ratcheting displacement.

3.4.4. *Displacement accumulation rates*

Figure 7 shows displacement accumulation per cycle as a function of the factor of safety $FS = \mu/\tan\eta$ for various

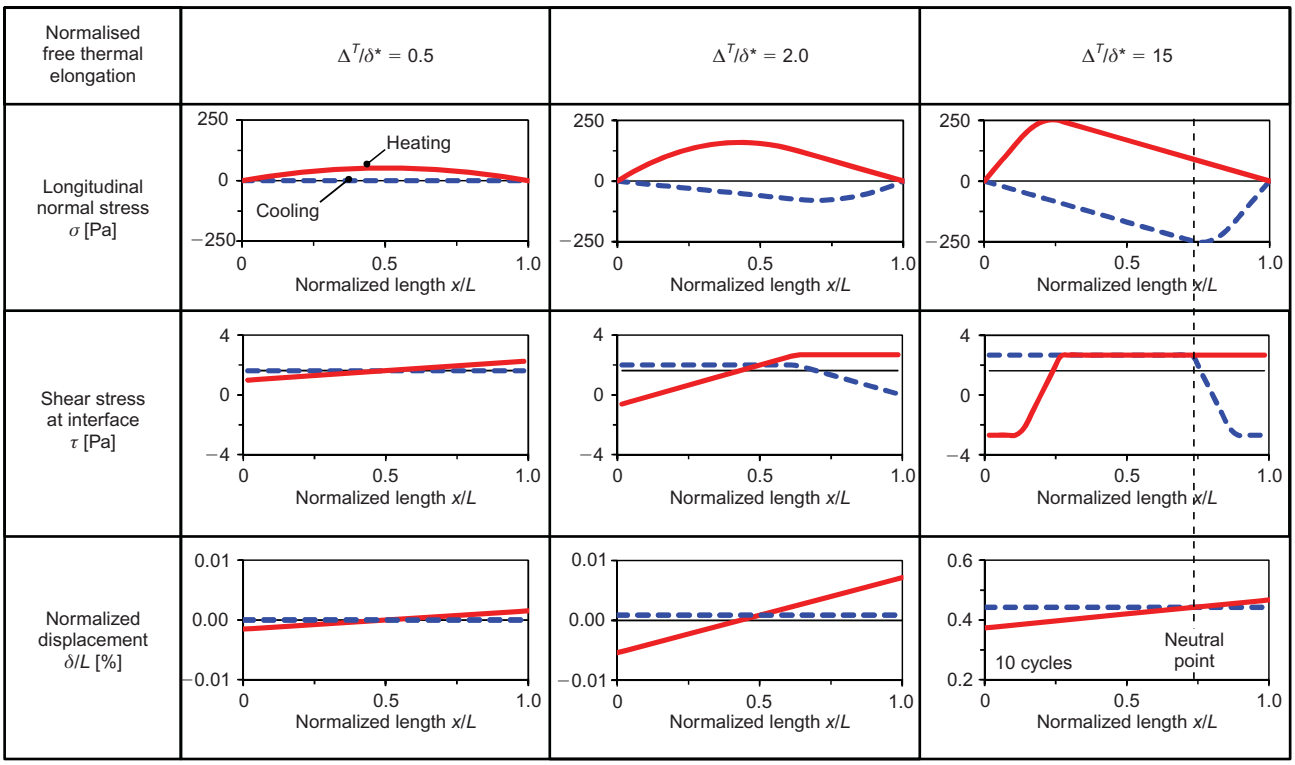

Figure 5. Characteristic load-transfer curves for cyclic temperature changes obtained with the numerical algorithm: longitudinal normal stress $\sigma = Q/(t_h \cdot B)$, shear stress at the interface τ, and normalized interface relative displacement δ/L. Continuous curves correspond to a heating phase and dotted lines to a cooling phase. Normalized free thermal elongation Δ^T/δ^* increases from left to right. Normalized displacement curves δ/L for $\Delta^T/\delta^* = 0.5$ and 2.0 are independent of the number of thermal cycles. Note: $FS = \mu/\tan\eta = 1.65$ and geomembrane parameters are found in Tables 1 and 2

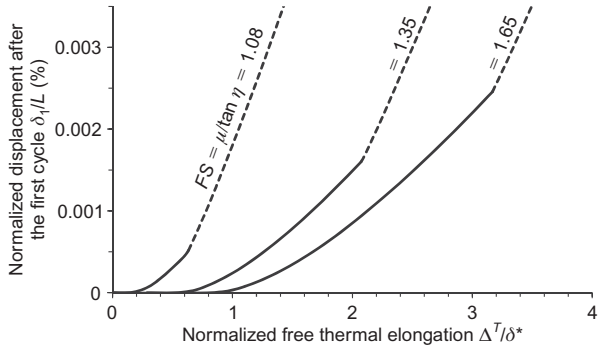

Figure 6. Normalized ratcheting displacement of the membrane upper edge δ_1/L after the first thermal cycle as a function of the normalized free thermal elongation Δ^T/δ^* and various static factors of safety $FS = \mu/\tan\eta$. Dotted lines indicate cases with accelerated ratcheting displacement. Note: geomembrane parameters are found in Tables 1 and 2

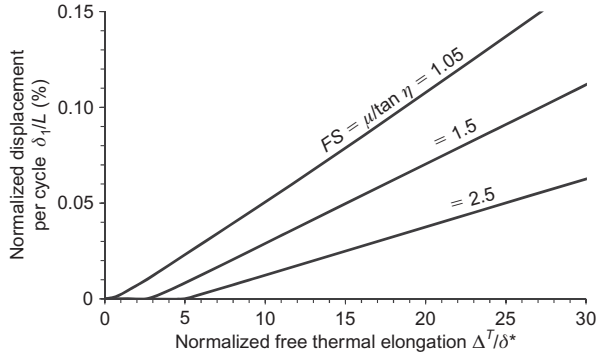

Figure 7. Ratcheting displacement per cycle of the membrane upper edge δ_1/L as a function of the static factor of safety $FS = \mu/\tan\eta$ for various values of the normalized free thermal elongation Δ^T/δ^*. Note: geomembrane parameters are found in Tables 1 and 2

values of the normalized free thermal elongation Δ^T/δ^*. The ratcheting displacement per thermal cycle increases as the static factor of safety FS decreases (i.e. steeper slopes) and the normalized free thermal elongation Δ^T/δ^* increases (i.e. high temperature changes ΔT or long membranes). For instance, a membrane on a slope with a factor of safety $FS = 1.5$ subjected to a normalized free thermal elongation $\Delta^T/\delta^* = 20$ (i.e. $\Delta T = 4°C$ for values in Tables 1 and 2) experiences an accumulated downward displacement $\Delta\delta_1 = 0.07\%\ L$ in every thermal cycle.

3.4.5. *Other observations*

The parametric study also shows that the membrane's width B, thickness t_h, Young's modulus E, and unit weight γ_m (buckling and wrinkle formation are not considered), as well as the first cycle polarity and the mean temperature slightly affect displacement accumulation rates. In contrast, the critical elastic interface displacement δ^* and the thermal expansion coefficient α are the most relevant parameters that control displacement accumulation. Governing dimensionless ratios are identified in Table 3.

4. DISCUSSION

4.1. Limitations of the models

The experimental model does not accurately represent field applications where high density polyethylene HDPE geomembranes are used to cover fine-grained soils and are restrained to prevent wind uplift (Giroud *et al.* 1995). However, these conditions can be analyzed numerically by choosing an appropriate critical elastic interface displacement and friction coefficient and by including additional axial forces in the formulation to represent restraint systems (Figure 3a).

The numerical model considers an elastic, perfectly plastic constitutive model for the interface whereas most interfaces have strain softening behavior (Dove and Frost 1999; Lemos and Vaughan 2000; Esterhuizen *et al.* 2001). This limitation can be overcome by implementing a strain softening constitutive model in Equation 5 defined by a peak and a residual strength. Since the ratcheting behavior is a strain-controlled process that involves small to medium strain levels, it is anticipated that a small strength reduction will occur at the interface of a smooth geomembrane (Koerner *et al.* 1986).

The critical elastic interface displacement can be estimated from a stress displacement curve of the geomembrane/base interface. However, the low vertical confinement of exposed geomembranes and small displacement levels involved require new test protocols to accurately measure this parameter. The adopted critical elastic interface displacement for the analysis of experimental data in this study ($\delta^* = 10$ μm) is consistent with the maximum peak to valley roughness of a smooth geomembrane on machine-finished metal (Hebeler 2005). For typical applications of geomembranes resting on fine-grained soils, the critical elastic interface displacement and the friction coefficient (or friction angle) increase primarily as a function of the geomembrane roughness (Fishman and Pal 1994). The precision of the image processing technique (0.03 mm) allows enough resolution to identify large accumulated displacements. Nevertheless, this limited precision does not allow study of the elastic behavior of the geomembrane/base interface.

Table 3. Governing dimensionless ratios

	Dimensionless ratios	
1	Relative geomembrane-to-interface stiffness	$(\gamma_m \cdot L^2/E)/\delta^*$
2	Normalized free thermal elongation	$\Delta^T/\delta^* = (\alpha \cdot \Delta T \cdot L)/\delta^*$
3	Normalized critical interface displacement	δ^*/t_h
4	Static factor of safety	$FS = \mu/\tan(\eta)$
5	Geomembrane slenderness	L/t_h

4.2. Example of field situation

The thermal expansion coefficient of HDPE geomembranes varies between 1.5 to $3.0 \cdot 10^{-4}$°C^{-1} depending on the roll direction (Pelte *et al.* 1994; Müller 2007), the friction coefficient of geomembrane/fine-grained soil interface may vary between 20° and 35° depending on the stress level, loading conditions, and interface texture (Seed and Boulanger 1991; Fishman and Pal 1994), and slopes of 2.5H: 1V are commonly lined using textured geomembranes.

For example, consider a HDPE geomembrane resting on a 2.5: 1 slope, so that $\eta \sim 22°$ (membrane length $L = 20$ m, thickness $t_h = 1.5$ mm, Young's modulus $E = 250$ MPa, thermal expansion coefficient $\alpha = 2 \cdot 10^{-4}$°C^{-1}, and interface friction coefficient $\mu = 0.47$). Numerical results using the algorithm described above indicate that temperature cycles with amplitude $\Delta T = 20$°C cause ratcheting displacement at a rate of 66 mm per thermal cycle when the critical interface displacement is $\delta^* = 1$ mm (smooth geomembrane/soil interface) and 49 mm per thermal cycle when $\delta^* = 10$ mm (rough geomembrane/soil interface).

4.3. General comments

The experimental modeling shows that ratcheting behavior can emerge when an exposed geomembrane is subjected to thermal cycles under idealized conditions. Further research can be conducted at a field scale to verify whether the phenomenon can occur.

Thermal ratcheting can be controlled in the short term by restraint systems, yet the performance of permanently exposed membranes can be compromised when decades of temperature cycles are involved. Other phenomena, such as membrane creep and anchored systems damage, could exacerbate thermally-induced permanent displacements in the long term.

Wrinkles tend to form towards the lower end of geomembranes (Chappel *et al.* 2012a, 2012b; Rowe *et al.* 2012b), which may be due to the high longitudinal normal stress that the numerical model predicts in that zone (Figure 5, $-x/L \sim 0.8$, $\Delta^T/\delta^* = 15$). The numerical model can be modified to account for wrinkle formation by including a critical longitudinal buckling force (Giroud and Morel 1992).

5. CONCLUSIONS

Exposed geomembranes expand and contract when subjected to cyclic thermal changes. Experimental results show that thermally-induced displacements in exposed geomembranes resting on inclined planes can result in the gradual accumulation of plastic downward displacements with the number of thermal cycles.

Governing equations are captured in a numerical algorithm that considers the thermo-elastic membrane properties, a constant temperature change amplitude, and a linear elastic-perfectly plastic constitutive model with a constant critical elastic displacement for the membrane–soil interface.

The membrane experiences accelerated downward ratcheting displacement when the critical elastic interface displacement δ^* is exceeded in more than half of the membrane length in a heating or cooling phase. The thermal elongation Δ^T required to overcome the critical interface displacement δ^* decreases as the inclination angle increases and the soil-membrane interface friction coefficient decreases. Thermally-induced ratcheting displacements increase as the factor of safety decreases (i.e. high base inclination angle η) and the interfacial friction μ decreases.

ACKNOWLEDGEMENTS

Support for this research was provided by the Fulbright US-Chile Equal Opportunities Scholarship Program, the US Department of Energy, and the Goizueta Foundation. F. Santamarina edited the manuscript.

NOTATIONS

Basic SI units are given in parentheses.

B	geomembrane width (m)
E	geomembrane Young's modulus (Pa)
FS	factor of safety (dimensionless)
k_j	interface shear stiffness (Pa/m)
L	geomembrane length (m)
L_0	length of discrete geomembrane element (m)
ΔL	geomembrane elongation (m)
N	number of discrete geomembrane elements (dimensionless)
P	period of temperature cycle (s)
Q	longitudinal force (N)
Q_i	longitudinal force on the ith element upper edge (N)
Q_{i+1}	longitudinal force on its lower edge (N)
S	shear force at the base interface (N)
t_h	geomembrane thickness (m)
W_i	weight of ith element (N)
α	thermal expansion coefficient of the geomembrane (°C^{-1})
γ_m	geomembrane unit weight (N/m^3)
δ	relative displacement (m)
δ^*	critical elastic interface displacement (m)
δ_i	downslope relative displacement of ith-element at its higher edge (m)
δ_{i+1}	downslope relative displacement of ith-element at its lower edge (m)
ε	tolerance value (N)
η	inclination of the base (°)
μ	interface friction coefficient (dimensionless)
τ	shear stress at the interface (Pa)
τ_{max}	shear strength at the interface (Pa)
φ	friction coefficient of the interface (°)
Δ_i	change in length of ith element (m)
ΔT	amplitude of temperature cycle (°C)
Δ^T	free thermal elongation of the geomembrane (m)
Δ_i^T	free thermal elongation of the ith element (m)
Δ_i^σ	elastic contraction of the ith element (m)

REFERENCES

Chappel, M., Brachman, R., Take, W. & Rowe, R. (2012a). Large-scale quantification of wrinkles in a smooth black HDPE geomembrane. *Journal of Geotechnical and Geoenvironmental Engineering*, **138**, No. 6, 671–679.

Chappel, M. J., Rowe, R. K., Brachman, R. W. I. & Take, W. A. (2012b). A comparison of geomembrane wrinkles for nine field cases. *Geosynthetics International*, **19**, No. 6, 453–469.

Dove, J. E. & Frost, J. D. (1999). Peak friction behavior of smooth geomembrane-particle interfaces. *Journal of Geotechnical and Geoenvironmental Engineering*, **125**, No. 7, 544–555.

Esterhuizen, J. J., Filz, G. M. & Duncan, J. M. (2001). Constitutive behavior of geosynthetic interfaces. *Journal of Geotechnical and Geoenvironmental Engineering*, **127**, No. 10, 834–840.

Fishman, K. L. & Pal, S. (1994). Further study of geomembrane/cohesive soil interface shear behavior. *Geotextiles and Geomembranes*, **13**, No. 9, 571–590.

Giroud, J., Pelte, T. & Bathurst, R. (1995). Uplift of geomembranes by wind. *Geosynthetics International*, **2**, No. 6, 897–952.

Giroud, J. P. & Morel, N. (1992). Analysis of geomembrane wrinkles. *Geotextiles and Geomembranes*, **11**, No. 3, 255–276.

Hebeler, G. L. (2005). *Multi-scale Behavior at Geomaterial Interfaces*. PhD thesis, Georgia Institute of Technology, Atlanta, GA, USA.

Koerner, R. M., Martin, J. P. & Koerner, G. R. (1986). Shear strength parameters between geomembranes and cohesive soils. *Geotextiles and Geomembranes*, **4**, No. 1, 21–30.

Lemos, L. & Vaughan, P. (2000). Clay–interface shear resistance. *Géotechnique*, **50**, No. 1, 55–64.

Müller, W. W. (2007). *HDPE Geomembranes in Gotechnics*. Springer, Heidelberg, Germany.

Pelte, T., Pierson, P. & Gourc, J. P. (1994). Thermal analysis of geomembranes exposed to solar radiation. *Geosynthetics International*, **1**, No. 1, 21–44.

Richardson, G. (2000). Exposed geomembrane covers: part 1 – geomembrane stresses. *GFR Magazine*, **18**, No. 7, 1–5.

Rowe, R. K. (2005). Long-term performance of contaminant barrier systems. *Géotechnique*, **55**, No. 9, 631–678.

Rowe, R. K. (2011). Short-and long-term leakage through composite liners. The 7th Arthur Casagrande Lecture. *Canadian Geotechnical Journal*, **49**, No. 2, 141–169.

Rowe, R. K., Chappel, M. J., Brachman, R. W. I. & Take, W. A. (2012a). Field study of wrinkles in a geomembrane at a composite liner test site. *Canadian Geotechnical Journal*, **49**, No. 10, 1196–1211.

Rowe, R. K., Yang, P., Chappel, M. J., Brachman, R. W. I. & Take, W. A. (2012b). Wrinkling of a geomembrane on a compacted clay liner on a slope. *Geotechnical Engineering Journal of the SEAGS & AGSSEA*, **43**, No. 3, 11–18.

Seed, R. B. & Boulanger, R. W. (1991). Smooth HDPE-clay liner interface shear strengths: compaction effects. *Journal of Geotechnical Engineering*, **117**, No. 4, 686–693.

Take, W., Watson, E., Brachman, R. & Rowe, R. (2012). Thermal expansion and contraction of geomembrane liners subjected to solar exposure and backfilling. *Journal of Geotechnical and Geoenvironmental Engineering*, **138**, No. 11, 1387–1397.

Take, W. A., Chappel, M. J., Brachman, R. W. I. & Rowe, R. K. (2007). Quantifying geomembrane wrinkles using aerial photography and digital image processing. *Geosynthetics International*, **14**, No. 4, 219–227.

The Editor welcomes discussion on all papers published in Geosynthetics International. Please email your contribution to discussion@geosynthetics-international.com by 15 June 2015.